

# Density Functional Theory Study of Silica Zeolite Structures: Stabilities and Mechanical Properties of SOD, LTA, CHA, MOR, and MFI

R. Astala, Scott M. Auerbach,\* and P. A. Monson†

Department of Chemical Engineering, Department of Chemistry, University of Massachusetts Amherst, Amherst, Massachusetts 01003

Received: February 11, 2004; In Final Form: April 9, 2004

We have investigated various silica zeolites using density functional theory with periodic supercells, plane waves, and pseudopotentials. These zeolitic phases include silica sodalite, chabazite, mordenite, silica LTA, and silicalite. Atom-level geometries, elastic properties, and cohesive energies are presented. Although the zeolites exhibit a wide range of Si–O–Si angles and densities, the cohesive energies remain nearly constant. The elastic properties vary significantly from one phase to another, and in some cases, large elastic anisotropies are observed.

## I. Introduction

Zeolites are nanoporous crystalline aluminosilicates frequently used in important chemical industry applications.<sup>1</sup> Their properties are determined by their nanoporous structures, which, in turn, are determined by the details of crystal growth processes. It is of great interest to understand the self-assembly and crystallization of zeolites, with a focus on discovering new ways to synthesize tailor-made pore structures. This issue is motivated by recent reports of silicalite crystallization from subcolloidal particles 3 nm in diameter.<sup>2,3</sup> A statistical mechanical model of these subcolloidal particles requires a general picture of silica structure and energetics, which we pursue in the present article. We perform density functional theory (DFT) calculations to identify essential physical aspects that a reliable model should include. In particular, we use DFT to compute quantities such as the bulk cohesive energy and elastic tensor components, which are useful in parametrizing classical force-field models.

Zeolites are built of a network of corner-sharing  $\text{TO}_4$  tetrahedra, where T = Si, Al, or other tetrahedrally coordinated atoms. For computational simplicity, we have investigated compositions consisting of only  $\text{SiO}_2$ , which avoids uncertainties regarding the locations of framework Al and charge-compensating species. In some cases, zeolites can be found with compositions approaching that of pure silica, e.g., silicalite. A remarkable property of silica is that it can form a number of different polymorphs, in which the local atomic coordinations are similar but the global networks formed are different. Zeolites, such as mordenite and silicalite, have relatively open structures, whereas naturally occurring polymorphs such as quartz and cristobalite are more dense. Moreover, the atom-level structure varies greatly from one polymorph to another. The Si–O–Si angles adopt values ranging from  $140^\circ$  to  $180^\circ$ , while the densities exhibit a similarly wide range of values. Therefore, it is interesting to investigate whether the cohesive energies depend strongly on the Si–O–Si angle distribution and whether the elastic properties can be correlated with density. Note that silica also exists in high-pressure phases that have 6-fold Si coordination, e.g., stishovite. Such phases are not investigated here.

The Si–O bonds in zeolites have polar covalent character (as discussed in ref 4). The atom-level properties of the material are determined by the bonding interactions between the Si and O atoms and by the long-ranged electrostatic field set up by the polarization of the Si–O bond. The properties are sensitive to the amount of charge transfer from Si to O. In ref 5, it is shown that rigid ion force-fields do not consistently reproduce the cohesive energies from one polymorph to the next. Density functional theory (DFT), which allows for the calculation of electron charge distributions in a self-consistent fashion, can however produce the properties of zeolites with high accuracy, as shown, e.g., in ref 6. The dense polymorphs of silica such as quartz, cristobalite, and tridymite have been studied extensively using first-principles methods.<sup>7–11</sup> Such results allow us to carefully benchmark the method, which we then apply to zeolites. Some earlier first-principles studies have been performed on zeolite polymorphs including sodalite, chabazite, and mordenite.<sup>6,8,11–13</sup> In the present work, we significantly extend the scope of first-principles calculations on silica polymorphs in two ways. Our calculations are made over a wider range of zeolites than has been considered previously, and for each structure considered, we make careful calculations of the mechanical properties in addition to the cohesive energy. By doing this, we establish essential physical ingredients required in building a model of silica over a wide range of conditions.

The remainder of this paper is organized as follows: In section II, we discuss the theoretical methods used in this work, with special attention to the calculation of elastic properties. In section III, the results for the zeolites are presented. First, a benchmarking of the method is performed by investigating dense phases such as  $\alpha$ - and  $\beta$ -quartz,  $\alpha$ - and  $\beta$ -cristobalite, and  $\beta$ -tridymite. We then proceed to study the low-density zeolitic polymorphs, which involve various kinds of nanoporosity. The zeolitic polymorphs are the main focus of this work; it is of interest to determine the cohesive energies and mechanical properties of these synthetic low-density phases from first principles. In section IV, the cohesive energies of the zeolites are discussed. These are found to be nearly independent of structure, despite large variations in local geometry. However, the elastic properties depend strongly on symmetry and network

\* To whom correspondence should be addressed. E-mail: auerbach@chem.umass.edu.

† E-mail: monson@ecs.umass.edu.

constraints imposed by the crystal structure. In the final section, we summarize and present closing remarks.

## II. Methods

Crystal structures of various zeolites are modeled using the periodic supercell approach. Total energies are optimized in two steps. First, internal coordinates of atoms and lattice parameters are relaxed to obtain an initial structure for more careful optimizations. Second, to correct for Pulay stress errors (see below) and to compute elastic tensor components, a series of calculations is performed in which lattice parameters are varied in a stepwise fashion while internal coordinates are relaxed for each set of lattice parameters. The very large MFI structure is optimized slightly differently. The first step is omitted, and the stepwise lattice parameter variation begins from the experimental structure. This is done to avoid an automated calculation of the stress tensor, which becomes highly computer-intensive for large structures. In all cases, crystal structures are constrained to the experimental space group symmetry (see also section II.B).

**A. Density Functional Methods.** Zeolites are modeled with density functional theory (DFT) using plane waves and pseudopotentials.<sup>14–16</sup> Calculations are performed using the VASP (Vienna ab initio simulation package) software developed at Institut für Materialphysik, Universität Vienna, Vienna, Austria.<sup>17–19</sup> The electron exchange–correlation potential is treated within the local density approximation (LDA) based on Ceperley–Alder data.<sup>20</sup> This functional has been found to accurately reproduce the structural properties of various dense 4-fold-coordinated silica polymorphs when compared to experimental data, as well as to calculations<sup>7</sup> performed using the generalized gradient GGA-PW-91 functional.<sup>21</sup> Below, we present comparisons between LDA and GGA-PW-91 results for  $\alpha$ - and  $\beta$ -quartz and  $\alpha$ - and  $\beta$ -cristobalite, as well as for silica SOD and CHA. The GGA-PW-91 functional has been found to reproduce the energy difference between stishovite (6-fold Si) and  $\alpha$ -quartz (4-fold Si) more accurately than does LDA.<sup>22</sup> Somewhat surprisingly, however, we show below that the GGA-PW-91 functional overestimates lattice parameters and underestimates cohesive energy differences of polymorphs with 4-fold Si coordination only. This superior performance of LDA for 4-fold Si is in agreement with results reported in ref 7. We report below that LDA also outperforms GGA-PW-91 for silica SOD and CHA. Therefore, the LDA functional is used throughout this work except when otherwise indicated.

Ion cores are modeled using the Vanderbilt-type ultrasoft pseudopotential included with the VASP software package.<sup>23,24</sup> In these potentials, the (2s, 2p) O and (3s, 3p) Si orbitals are included in the set of explicitly treated valence states. The normal ultrasoft versions of the pseudopotentials in the VASP database are used. The Brillouin zone is sampled using Monkhorst–Pack grids.<sup>25</sup> A  $3 \times 3 \times 3$  grid is used with quartz and cristobalite phases; a  $3 \times 3 \times 2$  grid with tridymite; a  $2 \times 2 \times 2$  grid with sodalite, chabazite, and LTA; and a  $2 \times 2 \times 1$  grid with mordenite; with MFI,  $\Gamma$ -point sampling is used. In most of the calculations, the plane-wave kinetic energy cutoff is set to 420 eV. However, with the large MFI structure, the 420 eV cutoff could not be used because of computer memory constraints. Instead, a cutoff of 380 eV is used. To obtain a proper reference value for the cohesive energy differences for both MFI and the other structures, the  $\alpha$ -quartz structure was optimized using both the 380 and 420 eV cutoff. The cohesive energies were found to be well converged at 380 eV; the error compared to 420 eV is less than 0.01 eV per  $\text{SiO}_2$  unit. The post-convergence 420 eV cutoff is used to reduce spurious Pulay

stresses that stem from the dependence of the plane-wave basis set on the lattice parameters.<sup>26</sup> Use of a larger cutoff value thus facilitates optimization of lattice parameters. Also, because the final geometries are obtained by performing a stepwise search for optimal lattice parameters, the effects of Pulay stresses on equilibrium structures are eliminated. For electron structure optimization, the convergence criterion is an energy change of 0.1 meV in total or less; for the internal coordinate optimization, the criterion is 0.02 meV per atom or less. Typically, this leads to maximum residual Hellmann–Feynman forces on atoms of significantly less than 0.1 eV per Å. In the stepwise lattice parameter optimization, the lattice parameters are varied in steps of 0.33% of the initial value.

The calculations are performed using PIII workstations and an Athlon PC cluster. A single-electron structure optimization cycle for a nine-atom  $\alpha$ -quartz unit cell takes approximately 2–3 CPU min on a PIII workstation. The same cycle for a 288-atom silicalite structure can take 10–20 CPU h using eight Athlon processors in parallel, and about 10 such cycles are required to optimize the internal coordinates of the atoms. However, because these computer resources are shared, these timings are only approximate.

**B. Mechanical Properties.** The mechanical properties of the polymorphs can be described by the elastic tensor  $\mathbf{C}$ .<sup>27</sup> Here, we use the standard convention where the elastic tensor is written as a  $6 \times 6$  matrix. The strain tensor can then be written as six-component vectors  $\vec{e}$ , where the components  $e_{1–3}$  describe pure strains and  $e_{4–6}$  describe pure shears. In the limit of small displacements, the internal energy change  $\Delta E$  per unit volume  $V_0$  at mechanical equilibrium can be written according to Hooke's law as

$$\Delta E/V_0 = \frac{1}{2} \sum_{ij=1}^6 C_{ij} e_i e_j \quad (1)$$

The stress tensor  $\mathbf{T}$  is also written as a six-component vector  $\vec{T}$ , where the components  $T_{1–3}$  describe normal stresses and  $T_{4–6}$  describe shear stresses. The stress tensor components  $T_j$  obey the relation

$$T_j = \sum_{i=1}^6 C_{ij} e_i \quad (2)$$

Because of crystallographic symmetries, elastic tensors typically have only a few independent components. If the equilibrium structure has space group symmetries, the energy, approximated as eq 1, must remain invariant under those symmetry transformations. In the case of cubic crystals, the number of independent components  $C_{ij}$  is reduced to four.

Our goal is to use the elastic tensor data in an auxiliary fashion to extract the zero-pressure and zero-temperature bulk modulus. Because we are interested in the bulk modulus at zero temperature, the thermal fluctuations can be ignored, and the symmetry of the structure can be constrained to the experimentally observed space group. Imposing the symmetry on the structure reduces the number of degrees of freedom of the system and therefore makes the calculation less computer intensive. This is especially important for zeolites with large unit cells, such as mordenite and silicalite. Thus, we are interested only in unit cell deformations that preserve the space group symmetry of a given polymorph. For consistency, space group symmetries are imposed for all structures.

The imposed space group symmetry constraints render some of the elastic tensor components redundant, because in most

**TABLE 1: Lattice Parameters, Si–O Distances (Å), and Si–O–Si Angles and O–Si–O Angles (deg) for  $\alpha$ -Quartz and  $\alpha$ -Cristobalite<sup>a</sup>**

	<i>a</i>	<i>c</i>	<i>d</i> (Si–O)	$\Theta$ (Si–O–Si)	$\Theta$ (O–Si–O)
$\alpha$ -quartz					
this work, LDA	4.89	5.39	1.60, 1.60	143.8	108.5–110.4
this work, PW-91	5.05	5.51	1.61, 1.62	150.5	108.7–110.0
DFT-LDA <sup>7</sup>	4.8992	5.3832	1.5987, 1.6045		108.8–110.4
DFT-LDA <sup>8</sup>	4.9541	5.4414	1.6061, 1.6092		
DFT-LDA <sup>9</sup>	4.8756	5.4052			
DFT-PW-91 <sup>7</sup>	5.0271	5.5089	1.6137, 1.6170		108.4–110.4
Hartree–Fock/6-311G(d) <sup>11</sup>	4.953	5.426	1.612*	145.3*	109.5*
experiment <sup>28</sup>	4.916	5.4054	1.605, 1.614	143.7	108.8–110.5
experiment <sup>29</sup>	4.9134	5.4052	1.608, 1.610	143.6	108.7–110.5
$\alpha$ -cristobalite					
this work, LDA	5.01	7.00	1.60	150.3	108.4–111.2
this work, PW-91	5.09	7.21	1.61	154.1	108.3–111.6
DFT-LDA <sup>7</sup>	4.9751	6.9261	1.5970, 1.5991	147.7	108.3–111.1
DFT-LDA <sup>8</sup>	5.0630	7.0823	1.6037		
DFT-LDA <sup>9</sup>	4.9586	6.9074			
DFT-PW-91 <sup>7</sup>	5.1190	7.1683	1.6144, 1.6146	154.2	108.7–111.2
Experiment <sup>30</sup>	4.9717	6.9222	1.603, 1.603	146.5	108.2–111.4

<sup>a</sup> An asterisk (\*) denotes an average.

cases the shears can be excluded and some lattice parameters are constrained to be equal. In the case of quartz and cristobalite, the *a* and *b* lattice parameters are constrained to be equal, so that  $e_1 = e_2$ , and therefore, a sum of components  $(C_{11} + C_{12} + C_{21} + C_{22})/2 = C_{11}^*$  is obtained. Such composite values are denoted by an asterisk (\*). In structures with cubic symmetry, such as sodalite and LTA, there is only one independent lattice parameter, and in these cases, only the bulk modulus (eq 3) is extracted.

The elastic tensor components are extracted by varying lattice parameters and mapping the total energy *E*. For most structures studied here, each independent lattice parameter is varied, and a quadratic fit to the total energy versus lattice parameter data is performed. Elastic tensor components are then proportional to the second derivative of the polynomial. The bulk modulus *K* is defined as

$$K = V_0 \left. \frac{d^2 E}{dV^2} \right|_{V=V_0} \quad (3)$$

where the volume change is induced by a uniform pressure *p* described by a stress tensor  $T_{1-3} = p$ ,  $T_{4-6} = 0$ . Assuming that the shear components  $e_{4-6}$  are zero due to symmetry constraints, upon inversion of eq 2, the bulk modulus becomes

$$K = \left( \sum_{i,j=1}^3 (\mathbf{C}^{-1})_{ij} \right)^{-1} \quad (4)$$

Despite the structural and elastic anisotropy present in many phases of silica, it is computationally more convenient to estimate bulk moduli by making isotropic volume changes. In particular, by shrinking and expanding the unit cell by the same amount in all directions and then recalculating the energy and hence the bulk modulus through eq 3, one arrives at an isotropic approximation to the bulk modulus, denoted  $K^i$ . In this case, the stress is induced by a uniform volume change described by the strain tensor  $e_{1-3} = dV/3$ ,  $e_{4-6} = 0$ . The difference in the values of *K* and  $K^i$  provides a measure of elastic anisotropy. Below, we explore the magnitude of error that arises when this isotropic approximation is made for anisotropic silicates.

### III. Results

In the next three subsections, the results obtained for various polymorphs are presented. In subsection III.A, the properties

of naturally occurring high-density silica phases are computed for purposes of benchmarking the DFT method, while in subsection III.B, the zeolitic low-density polymorphs are investigated. In subsection III.C, the cohesive energies of different polymorphs are presented.

**A. Benchmarking the Method: Dense Polymorphs.** To model the properties of zeolites using DFT methods, one must decide which exchange-correlation functional to use and also confirm that the plane-wave cutoff energy and *k*-point density are sufficient to obtain accurate results. A convenient way to do this is to calculate the structural and mechanical properties of dense silica phases with relatively small unit cells and then perform a comparison to earlier experimental and theoretical results. In addition, by calculating the properties of such phases, a comparison between the properties of zeolites and dense polymorphs can be made. We performed this benchmarking on  $\alpha$ -quartz,  $\beta$ -quartz,  $\alpha$ -cristobalite,  $\beta$ -cristobalite, and  $\beta$ -tridymite. Overall, the agreement between our calculations and previously reported data is excellent for all five dense phases. In what follows, we detail results for the mechanical properties of  $\alpha$ -quartz and  $\alpha$ -cristobalite, because experimental bulk moduli are readily available for these phases. The remaining details for all of the dense phases are presented as Supporting Information.

The  $\alpha$ -quartz structure has a trigonal nine-atom unit cell with a space group symmetry of  $P3_221$ , or equivalently  $P3_121$ . In this work, we use a hexagonal nine-atom unit cell that is constrained to this symmetry. Table 1 shows the excellent agreement between our present results and previous DFT calculations on  $\alpha$ -quartz. The bulk modulus and elastic tensor components for  $\alpha$ -quartz agree well with experimental results (Table 2). The isotropic approximation overestimates the bulk modulus by only 1 GPa out of 38 GPa.

$\alpha$ -Cristobalite has a tetragonal unit cell with a space group symmetry of  $P4_22_2$ . The calculation is performed using 12-atom unit cells. The  $\alpha$ -cristobalite has the lowest bulk modulus of all of the structures investigated here. As a technical consequence of these small bulk moduli, large strains are required to obtain reliable data because the energy changes by only a small amount upon compression. However, for larger strains, the quadratic fit becomes less accurate; instead, we used a cubic fit to obtain the second derivative at equilibrium. The elastic tensor of  $\alpha$ -cristobalite is found to be relatively isotropic.

**TABLE 2: Bulk Moduli ( $K$ ) and Isotropic Approximation to Bulk Moduli ( $K^i$ ), as Well as Elastic Tensor Components, of  $\alpha$ -Quartz and  $\alpha$ -Cristobalite (in Units of GPa)**

	$K$	$K^i$	$C_{11}^*$	$C_{33}$	$C_{13}$
$\alpha$ -quartz					
this work, LDA	38	39	95	113	11
DFT-LDA <sup>10</sup>	42.8		102	97	21
experiment <sup>31</sup>	38.98		97.16	109.19	13.02
$\alpha$ -cristobalite					
this work, LDA	8	10	49	39	-12
experiment <sup>32</sup>	15.95		63.2	42.4	-4.4
experiment <sup>30</sup>	11.5				

As such, the isotropic approximation overestimates the bulk modulus of  $\alpha$ -cristobalite by 2 GPa out of 8 GPa.

**B. Siliceous Zeolitic Frameworks:**<sup>33</sup> **SOD, CHA, MOR, LTA, MFI.** Next, we return our focus to silica zeolites. The aim is to investigate how cohesive energies and bulk moduli depend on densities and bond angle distributions.

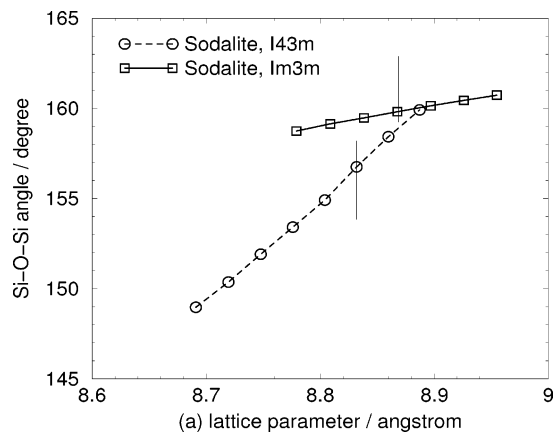
*I. Silica SOD.* Sodalite is an important zeolite because it forms a building block of more complex materials such as LTA and FAU.<sup>33</sup> Therefore, by investigating the properties of a sodalite cage, one can gain insights into the behavior of these more complex and technologically important zeolites. Sodalite has been studied previously using periodic first-principles calculations.<sup>8,13,34</sup>

All-silica sodalite has a highly symmetric body-centered-cubic structure with 36 atoms per unit cell. The space group of the structure has been determined to be  $Im\bar{3}m$ .<sup>35</sup> However, in the experimental setup, the structure contained encapsulated ethylene glycol in the sodalite cages, which might have led to an expanded high-symmetry structure. Furthermore, small deviations that would reduce the space group to  $I\bar{4}3m$  have been observed. Such deviations stem from a relaxation of the O atoms from (0yy)- to (xyy)-type positions. At low temperatures, below 220 K, this structure was found to relax toward a monoclinic low-symmetry phase. In both  $Im\bar{3}m$  and  $I\bar{4}3m$  phases, sodalite has a single set of symmetry-equivalent Si–O–Si angles.

In this work, both the  $I\bar{4}3m$  and  $Im\bar{3}m$  structures are investigated. The  $I\bar{4}3m$  structure is slightly more stable, by 0.002 eV per  $\text{SiO}_2$ . In both structures, all Si–O–Si angles have equal values because of the space group symmetries. Equilibrium lattice parameters and structural properties are listed in Table 3. The LDA results are in good agreement with experiment, whereas the GGA-PW-91 functional produces lattice parameters that are too large. The behavior of the Si–O–Si angles as a function of the lattice parameter is shown in Figure 1 for these two structures. As the unit cell is expanded, the two Si–O–Si angles approach each other, whereas during compression, the angle in the  $I\bar{4}3m$  structure decreases more rapidly. As a result, the  $I\bar{4}3m$  structure is significantly less rigid, with a bulk modulus of  $K = 18$  GPa. On the other hand, the  $Im\bar{3}m$  phase gives a bulk modulus of 93 GPa. The latter bulk modulus is high because the symmetry constraints fix the structure into a saddle-point configuration on the potential energy surface, in which collective rotation of  $\text{SiO}_4$  tetrahedra is symmetry forbidden.

**TABLE 3: Lattice Parameters and Si–O Distances ( $\text{\AA}$ ), O Special Positions (in Internal Coordinates), and Si–O–Si and O–Si–O Angles (deg) for Sodalite**

	$a$	$d(\text{Si–O})$	O $x$	O $y$	$\Theta(\text{Si–O–Si})$	$\Theta(\text{O–Si–O})$
this work, LDA, $I\bar{4}3m$	8.83	1.59	-0.0197	0.6466	156.7	109.1–110.1
this work, LDA, $Im\bar{3}m$	8.87	1.59	0	0.6473	159.8	109.1, 110.2
this work, PW-91, $I\bar{4}3m$	8.92	1.62	-0.0261	0.6461	154.7	109.2–110.0
this work, PW-91, $Im\bar{3}m$	8.96	1.61	0	0.6475	159.3	109.0, 110.4
DFT-LDA, <sup>8</sup> $Im\bar{3}m$	8.9431	1.6068	0	0.6477	159.6	
experiment, <sup>35</sup> $Im\bar{3}m$	8.8273	1.586	0	0.6474		110.4

**Figure 1.** Behavior of Si–O–Si bond angles in the  $I\bar{4}3m$  and  $Im\bar{3}m$  sodalite structures as the  $a$  lattice parameter is varied. Vertical lines denote the equilibrium structures, and the curves are only to guide the eye.

The value for the  $Im\bar{3}m$  phase is somewhat lower than 122 GPa reported in ref 8. A possible explanation is the difficulty in obtaining basis set convergence while using norm-conserving pseudopotentials for O atoms, as was done in ref 8.

These results suggest that the compressed  $I\bar{4}3m$  structure could exist as an intermediate-temperature phase before the transformation to the low-symmetry monoclinic phase takes place. The  $I\bar{4}3m$  sodalite is favored over the  $Im\bar{3}m$  sodalite at higher pressures because of its lower bulk modulus, which allows the structure to become more dense. Such behavior has indeed been observed in a high-pressure X-ray and neutron powder diffraction study of silica sodalite containing encapsulated 1,3-dioxolane template molecules.<sup>36</sup>

*2. Silica CHA.* Chabazite is an interesting zeolite because it has a more complicated structure than sodalite and a more open framework. The difference is that, in chabazite,  $\text{SiO}_4$  tetrahedra are linked to form a network with four crystallographically distinct Si–O–Si angles. Therefore, the response to external stress is likely to be more complex. Earlier periodic first-principles calculations of chabazite have been reported in refs 11–13.

All-silica chabazite has a rhombohedral unit cell that contains 36 atoms. The space group symmetry of chabazite is  $R\bar{3}m$ . The space group symmetry allows shear distortions as the rhombohedral angle  $\gamma$  is varied. To calculate the equilibrium value of  $\gamma$  and also to obtain the bulk modulus, the total energy surface is mapped as a function of  $a$  and  $\gamma$ . At each point, the internal coordinates are relaxed. The bulk modulus is extracted by calculating the  $dE^2/d^2V$  along the minimum-energy path on this surface.

Lattice parameters of the relaxed chabazite structure are in good agreement with experimental data (Table 4). They are slightly underestimated with the LDA and slightly overestimated with the GGA-PW-91 functional. The LDA equilibrium volume is  $778 \text{ \AA}^3$ , whereas the PW-91 value is  $806 \text{ \AA}^3$ . This is in agreement with the DFT-PW-91 value of  $807.9 \text{ \AA}^3$  reported in

**TABLE 4: Lattice Parameters  $a$  (Å) and  $\gamma$  (deg), Si–O Bond Lengths (Å), and O–Si–O Angles (deg) for Chabazite<sup>a</sup>**

	$a$	$\gamma$	$d(\text{Si-O})$	$\Theta(\text{O-Si-O})$
this work, LDA	9.22	$94.2 \pm 0.7$	1.59–1.60	109.0–110.0
this work, PW-91	9.33	$94.4 \pm 0.7$	1.61–1.62	108.7–110.2
Hartree–Fock/6-31G(d) <sup>11</sup>	9.319	94.7	1.613*	109.5*
experiment <sup>37</sup>	9.291	93.9		

<sup>a</sup> An asterisk (\*) denotes an average.

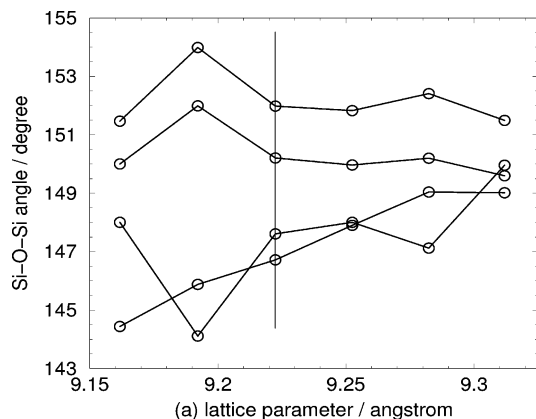


**Figure 2.** Behavior of Si–O–Si angles in chabazite as the  $a$  lattice parameter is varied. Vertical line denotes the equilibrium structure, and the different curves, only to guide the eye, correspond to different angles.

**TABLE 5:  $a$ ,  $c$  (Å), and  $\gamma$  (deg) Lattice Parameters for the Centrosymmetric Unit Cell of Mordenite, as Well as Si–O Bond Lengths (Å) and O–Si–O Angles (deg)**

	$a$	$c$	$\gamma$	$d(\text{Si-O})$	$\Theta(\text{O-Si-O})$
this work, LDA	13.6	7.47	$97.6 \pm 0.2$	1.59–1.60	108.4–110.7
DFT-LDA <sup>6</sup>	13.674	7.526	97.12	1.596–1.612	108.0–110.9
DFT-PW-91 <sup>6</sup>	13.804	7.606	97.18	1.610–1.630	107.7–111.3
experiment <sup>38 a</sup>	13.678	7.524	97.18	1.587–1.649	105.5–113.0
experiment <sup>39</sup>	13.537	7.482	96.99	1.583–1.664	104.8–112.9

<sup>a</sup> Using  $Cmcm$  framework symmetry.

ref 12. Our results indicate that the rhombohedral angle  $\gamma$  remains fairly constant as the lattice parameter  $a$  is varied. The Si–O–Si angles show complicated patterns of relaxation as the unit cell is compressed (Figure 2). One set of bond angles tends to decrease uniformly, whereas the three other sets behave in a nonsystematic fashion, suggesting that more complex coordinates are required to understand how chabazite responds to pressure. The bulk modulus is large, 59 GPa, indicating that there is no cooperative mode of  $\text{SiO}_4$  tetrahedra rotation that would allow an easy path for compression.

3. *Silica MOR.* Next, we proceed to even more complex zeolites. In mordenite the  $\text{SiO}_4$  network forms a structure which has a wide range of Si–O–Si angles, up to 180 degrees. Therefore it is interesting to study whether this spread of values affects the cohesive energy. This zeolite has been studied earlier by periodic DFT calculations in ref 6.

Mordenite has an orthorhombic unit cell with a framework space group symmetry of  $Cmcm$ , which however might decrease to  $Cmc2_1$  because of the effect of extraframework atoms.<sup>38</sup> In this work, a centrosymmetric  $Cmcm$  72-atom unit cell is used. With this particular unit cell choice, the lattice parameters  $a$  and  $b$  are equal, and the angle  $\gamma$  between them can vary.

The lattice parameters are in good agreement with experimental data (Table 5). However, experimental structures exhibit a somewhat wider range of Si–O bond lengths than those observed in this work and in earlier theoretical studies.<sup>6</sup>

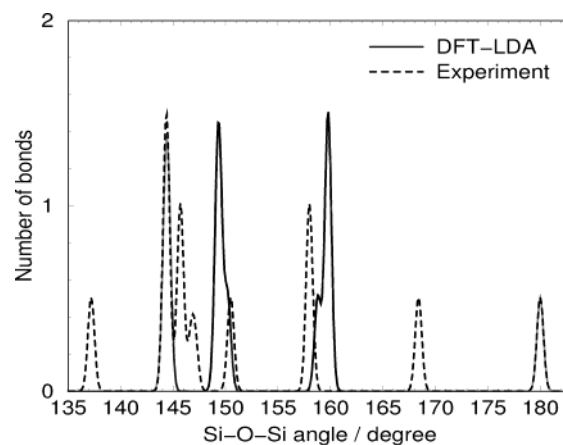


**Figure 3.** Si–O–Si bond angle distribution in mordenite. The experimental data from ref 38 and results from present calculations are shown. The peaks have been smeared by performing a convolution with a Gaussian function to simplify the presentation.

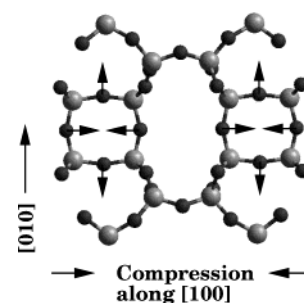


**Figure 4.** Pattern of relaxation of the 4-rings when mordenite is being compressed along [100] axis.

**TABLE 6: Bulk and Isotropic Moduli, as Well as Elastic Tensor Components, of Mordenite (in GPa)**

	$K$	$K^I$	$C_{11}$	$C_{22}$	$C_{33}$	$C_{12}$	$C_{13}$	$C_{23}$
mordenite, LDA	57	72	59	137	206	64	38	34

The distribution of Si–O–Si angles in the relaxed structure is plotted in Figure 3. In comparison, experimental data for natural mordenite from ref 38, assuming  $Cmcm$  framework symmetry, are also presented. The experimental data show a minimum Si–O–Si angle, of  $137.3^\circ$ , whereas DFT-LDA gives a lowest value of  $144.2^\circ$ . Also, in the experimental structure, there is a set of Si–O–Si triplets with an angle of  $168.5^\circ$  participating in 4-rings, whereas in the DFT-LDA relaxed structure, these angles have a lower value of  $158.9^\circ$ . These differences can be explained by the presence of extraframework  $\text{H}_2\text{O}$  molecules in the experimental sample. Furthermore, the  $158.9^\circ$  Si–O–Si angle is highly sensitive to changes in the  $a$  lattice parameter. When the crystal is compressed or expanded in the soft [100] direction, the 4-ring to which the Si–O–Si triplets belong shows significant relaxation (Figure 4). Thus, a small lattice expansion due to hydration in the experimental setup might lead to the discrepancy. In contrast, when the strain is applied in the [010] or [001] directions, the Si–O–Si angle distribution changes by only a small amount.

The elastic tensor of mordenite is highly anisotropic, with the [100] direction being the softest while the [010] and [001] directions are more rigid (Table 6). Thus, the value of the bulk modulus is largely determined by the  $C_{11}$  elastic constant. The value of  $K$  obtained here is lower than the calculated value of 74.04 GPa reported in ref 6. In that work, the elastic tensor components were not explicitly calculated; instead, a series of fixed-volume calculations was performed, which can lead to

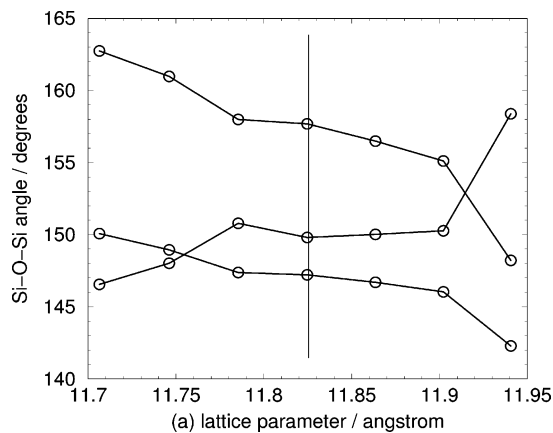


**Figure 5.** Behavior of Si–O–Si angles in LTA as the  $a$  lattice parameter is varied. The vertical line denotes the equilibrium structure, and the curves, only to guide the eye, correspond to different angles.

**TABLE 7: Lattice Parameter, Si–O Bond Lengths, and O–Si–O Angles for LTA**

	$a$ (Å)	$d(\text{Si–O})$ (Å)	$\Theta(\text{O–Si–O})$ (deg)
LTA, LDA	11.9	1.58–1.60	108.7–109.7

**TABLE 8: Lattice Parameters (Å), Si–O Bond Lengths (Å), and O–Si–O Angles (deg) for Orthorhombic MFI**

	$a$	$b$	$c$	$d(\text{Si–O})$	$\Theta(\text{O–Si–O})$
this work, LDA	20.1	19.9	13.4	1.59–1.61	107.9–110.9
experiment <sup>45</sup>	20.087	19.894	13.372	1.570–1.601	107.1–111.5

errors due to the large elastic anisotropy. This effect is clearly seen when comparing the bulk modulus ( $K = 57$  GPa) to the modulus for isotropic volume change ( $K^i = 72$  GPa).

**4. Silica LTA.** The LTA framework consists of connected sodalite cages in a cubic arrangement.<sup>40</sup> High-silica forms of LTA are known as ZK-4. These have been synthesized with Si/Al ratios as high as 1.7.<sup>41</sup> Here, a hypothetical all-silica LTA structure with a space group symmetry of  $Pm\bar{3}m$  is studied. In our earlier publication, this structure was used as a simplified model of aluminosilicate LTA.<sup>42</sup> Silica LTA has 72 atoms per unit cell and three sets of symmetry-inequivalent Si–O–Si angles.

The lattice parameter, Si–O bond lengths, and O–Si–O angles of the relaxed structure are presented in Table 7. The framework is constrained by the symmetry so that the Si–O–Si angles cannot relax easily in a cooperative fashion. This behavior is shown in Figure 5. Also, the bulk modulus of LTA is fairly high, 46 GPa.

**5. Silica MFI.** The most complex zeolite studied in this paper is siliceous MFI, which has 288-atom unit cell and, as with mordenite, a wide range of Si–O–Si angles. We are not aware of an earlier first-principles periodic calculation of MFI zeolite.

The high-silica MFI has different structures, depending on the temperature and whether the crystal has been calcined.<sup>43–45</sup> At high temperatures and in the as-synthesized form, where tetrapropylammonium (TPA) cations occupy the channel junctions, the crystal has orthorhombic  $Pnma$  space group symmetry. At low temperatures, a displacive phase transformation into a monoclinic symmetry takes place.<sup>46</sup> Here, the high-temperature orthorhombic phase of silicalite (siliceous MFI) is investigated. Lattice parameters and Si–O bond lengths of the relaxed structure are listed in Table 8. The DFT-LDA calculations agree well with the experimental data. Distributions of Si–O–Si angles for the computed and experimental structures are shown in Figure 6. The two distributions mostly agree. Notably, in

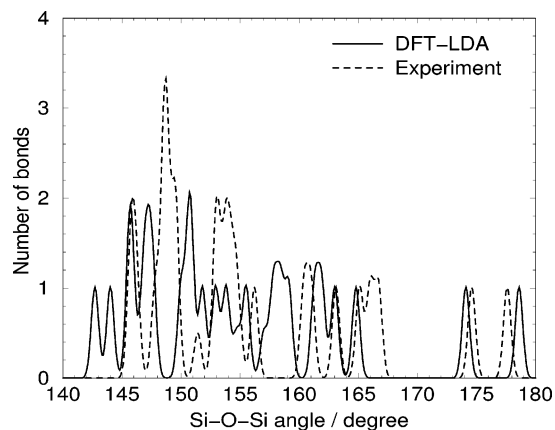


**Figure 6.** Si–O–Si bond angle distribution in the calcined orthorhombic MFI. The experimental data from ref 45 and results from present calculations are shown. The peaks have been smeared by performing a convolution with a Gaussian function to simplify the presentation.

**TABLE 9: Bulk Modulus  $K$  and the Elastic Tensor Components of Silicalite (in GPa)**

	$K$	$C_{11}$	$C_{22}$	$C_{33}$	$C_{12}$	$C_{13}$	$C_{23}$
silicalite, LDA	41	179	101	140	–29	29	–2

**TABLE 10: Cohesive Energies of the Different Polymorphs Relative to  $\alpha$ -Quartz<sup>a</sup>**

structure	cohesive energy (eV/SiO <sub>2</sub> )			Si–O–Si angle distribution (deg)	
	this work		experiment	LDA	PW-91
	LDA	PW-91		LDA	PW-91
$\alpha$ -quartz	0	0		143.8	150.5
$\beta$ -quartz	0.02	0.00		154.0	154.3
$\alpha$ -cristobalite	0.03	–0.03	0.029 <sup>48</sup>	150.3	154.1
$\beta$ -cristobalite	0.03	–0.04		151.3	152.3
$\beta$ -tridymite	0.04			180.0	
sodalite $I43m$	0.05	–0.02		156.7	154.7
sodalite $Im\bar{3}m$	0.05	–0.02		159.8	159.3
chabazite	0.07	0.00	0.118 $\pm$ 0.016 <sup>49</sup>	146.7–152.0	146.8–151.4
mordenite	0.05			144.2–180.0	
LTA	0.08			147.2–157.7	
silicalite	0.05		0.070 $\pm$ 0.008 <sup>49</sup>	142.7–178.6	

<sup>a</sup> Room-temperature experimental enthalpies of formation (ref 49 and as cited in ref 48) are also listed for some structures.

the calculated structure, the majority of the angles are between 142° and 165°, whereas in the experimental structure, the range is from 145° and 168°, indicating a small shift. In both cases, some Si–O–Si angles have values as large as 173–179°. The internal coordinates of the relaxed asymmetric unit are listed in the Supporting Information.

The bulk modulus (41 GPa) and the elastic tensor components of silicalite are listed in Table 9. The structure has anisotropic elastic properties with the [100] axis being the most rigid and the [010] axis being the softest. The experimental result for Young's modulus, i.e., the ratio of uniaxial stress to uniaxial strain, is 3–5 GPa in the [100] and [010] directions.<sup>47</sup> Our calculated values are significantly larger: 162 GPa in the [100] direction and 96 GPa in the [010] direction. The difference might stem from the high space group symmetry that was assumed in the calculation, which prevents the collapse of the crystal to a lower-symmetry structure. Furthermore, the experimental samples were twinned crystals that might have greater flexibility.

**C. Cohesive Energies.** Cohesive energies of the different polymorphs (per SiO<sub>2</sub>, relative to  $\alpha$ -quartz) are listed in Table 10. The values are very small, suggesting that the cohesive energies of silica zeolites are almost independent of structure

**TABLE 11: Volume per SiO<sub>2</sub> Unit (Å<sup>3</sup>) in Different Silica Polymorphs Calculated Using DFT-LDA and DFT-PW-91 Methods**

structure	LDA	PW-91	experiment <sup>a</sup>
α-quartz	37	41	37.7
β-quartz	40	42	39.4
α-cristobalite	44	47	42.8
β-cristobalite	45	47	45.3
β-tridymite	49		45.9
sodalite <i>I43m</i>	57	59	
sodalite <i>Im3m</i>	58	60	57.3–57.4
chabazite	65	67	66.5
mordenite	57		58.2, 56.7
LTA	69		
silicalite	56		55.6

<sup>a</sup> Experimental values calculated from the lattice parameters tabulated above and in the Supporting Information.

and density. The naturally occurring polymorphs, β-quartz, α-cristobalite, and β-cristobalite, have slightly lower energies than do the synthetic low-density phases. Interestingly, the cohesive energies are almost constant, even for the structures with very high Si–O–Si angles, such as β-tridymite, or structures with broad Si–O–Si angle distributions, such as mordenite and silicalite. The results also show that the agreement between the LDA results and experimental data is fairly good, considering how small the relative cohesive energies are. However, the GGA-PW-91 appears to underestimate the cohesive energy differences and even predicts that the most stable polymorph is β-cristobalite, rather than α-quartz. The origin of this behavior is not clear and needs to be investigated further.

#### IV. Discussion

Cohesive energies of the different zeolites and dense polymorphs are remarkably independent of the local atomic structure and, in particular, of the Si–O–Si angle distribution. The Si–O bond lengths have almost constant values at about 1.6 Å, and the O–Si–O angles are generally close to the tetrahedral angle of 109.5°. However, Si–O–Si angles can vary from 140° to 180°, and the densities of the structures vary widely (Table 11). Some correlation between the density and cohesive energy appears to be present, as observed earlier both experimentally<sup>50</sup> and theoretically.<sup>51</sup> For instance, the two least dense polymorphs, chabazite and LTA, also have the highest cohesive energies. The reliability of this correlation warrants further investigation.

The bulk moduli of the different polymorphs show no correlation with density. This can be seen by comparing polymorphs for which the densities are almost the same, such as sodalite and mordenite: the bulk moduli differ by a large factor. Instead, the network and space group symmetry constraints in a particular structure play an important role. They determine whether Si–O–Si angles are free to relax in modes that involve rotations of SiO<sub>4</sub> tetrahedra.<sup>52</sup> The effect of symmetry becomes clear when pairs of structures with the same network connectivity but with different space groups, such as *I43m* sodalite and *Im3m* sodalite, are found to have very different bulk moduli. Often, in such cases, one of the configurations is a saddle-point structure. The bulk modulus becomes artificially high because of the constraints required to stabilize this symmetry during energy minimization.

For most structures, the elastic properties are anisotropic. The softness under uniaxial strain is accompanied by large relaxations of Si–O–Si angles, whereas strain along rigid directions leads to only small relaxation. Such behavior is evident, e.g., in mordenite, where large relaxations of the Si–O–Si angles

are observed as the strain is applied along the [100] direction. To understand the elastic properties and to obtain an accurate value for the bulk modulus, an explicit calculation of the elastic tensor components is required. Making the isotropic approximation gives an estimate of the bulk modulus that is uniformly higher than the actual bulk modulus, by as much as 30% in our calculation above.

When external stress is applied, the most important relaxation mechanism is the change in Si–O–Si angles, whereas the relaxation of O–Si–O angles or Si–O bond lengths is less prevalent. The bulk moduli for all the structures are relative large. This leads to an apparent paradox: why is there a large energy penalty for deforming the structure of any *particular* polymorph, even though the cohesive energies of the *different* polymorphs that have very different structures are almost equal? Despite this apparent paradox, the fact remains that a reliable model of silica must reproduce the following results of our DFT calculations: (i) cohesive energies should vary little from one polymorph to the next, and (ii) bulk moduli should be relatively large and sensitive to network constraints.

In what follows, we speculate on how to build models that satisfy these criteria. Models vary in complexity. We begin by discussing simple models and then proceed to more sophisticated ones. A very simple model of a zeolite is an assembly of corner-sharing rigid SiO<sub>4</sub> tetrahedra. This model can satisfy the criterion of almost equal cohesive energies. However, it is easy to show that, with such a model, some phases such as α-cristobalite are no longer mechanically stable at nonzero pressures because there exist deformation paths involving only rigid-body rotations and translations of tetrahedra. This problem can be tackled by adding an Si–O–Si bond-bending term to the potential energy expression; we are presently investigating such models. Also, to account for the full range of bulk moduli for different zeolites and to avoid overly high values of the bulk modulus, some flexibility of tetrahedra has to be allowed. These approaches have similarities to the rigid-unit models used in ref 52.

For modeling subcolloidal silica nanoparticles, which are often negatively charged under alkaline conditions, atomistic models are likely required. Typically the Si–O bonding is modeled by Born–Meyer-type potentials that have short-ranged repulsion and electrostatic attraction between Si and O. However, with rigid-ion pair potentials, it is difficult to obtain accurate cohesive energies, as shown in ref 5. In that work, a range of both dense and zeolitic polymorphs was modeled using both rigid-ion and shell model potentials, and a comparison with experimental structural and cohesive energy data was performed. The shell models generally gave better agreement with experimental data. Empirical force-field calculations have also been performed to compute the elastic properties of silica polymorphs.<sup>53–55</sup> Accurate results can be obtained if experimental elasticity data are used for parameter fitting. However, it is not clear whether these force fields can reproduce the cohesive energies accurately for a wide range of zeolites.

#### V. Conclusions

Calculations of various silica zeolites using DFT-LDA plane-wave pseudopotential techniques were performed. The structures included are silica sodalite, chabazite, mordenite, silica LTA, and silicalite. Furthermore, α- and β-quartz, α- and β-cristobalite, and β-tridymite were investigated to perform benchmarking and comparisons. The equilibrium geometries, elastic properties, and cohesive energies were calculated. The cohesive energies are almost independent of structure, despite large variations in the Si–O–Si angle distribution among the different

polymorphs. Bulk moduli were found to depend strongly on network constraints and space group symmetry. These factors determine whether the Si—O—Si angles can relax in a cooperative fashion to relieve stress. Furthermore, large elastic anisotropy was observed.

Several interesting questions about the electronic structure in these systems remain to be investigated. For example, it is of interest to study the extent to which Si—O bond polarization varies from site to site or from polymorph to polymorph. Further calculations are required to address such issues.

These results show that, for an empirical potential to be transferable, it must obey the condition that cohesive energy differences are small while bulk moduli are large. The results presented here can be used to test the reliability of such models.

**Acknowledgment.** This work was supported by a grant from the National Science Foundation (CTS-0103010).

**Supporting Information Available:** Structural properties of dense  $\beta$ -phases and internal coordinates of silica MFI. This material is free of charge via the Internet at <http://pubs.acs.org>.

## References and Notes

- (1) *Handbook of Zeolite Science and Technology*; Auerbach, S. M., Carrado, K. A., Dutta, P. K., Eds.; Marcel Dekker: New York, 2003.
- (2) Kragten, D. D.; Fedeyko, J. M.; Sawant, K. R.; Rimer, J. D.; Vlachos, D. G.; Lobo, R. F.; Tsapatsis, M. *J. Phys. Chem. B* **2003**, *107*, 10006.
- (3) Ravishankar, R.; Kirshhock, C. E. A.; Knops-Gerrits, P.-P.; Feijen, E. J. P.; Grobet, P. J.; Vanoppen, P.; De Schryver, F. C.; Mieke, G.; Fuess, H.; Schoeman, B. J.; Jacobs, P. A.; Martens, J. A. *J. Phys. Chem. B* **1999**, *103*, 4960.
- (4) Rozanska X.; van Santen R. A. In *Handbook of Zeolite Science and Technology*; Auerbach, S. M., Carrado, K. A., Dutta, P. K., Eds.; Marcel Dekker: New York, 2003; p 785.
- (5) de Boer, K.; Jansen, A. P. J.; van Santen, R. A. *Phys. Rev. B* **1995**, *52*, 12579.
- (6) Demuth, T.; Hafner, J.; Benco, L.; Toulhoat, H. *J. Phys. Chem. B* **2000**, *104*, 4593.
- (7) Demuth, Th.; Jeanvoine, Y.; Hafner, J.; Ángyán, J. G. *J. Phys.: Condens. Matter* **1999**, *11*, 3833.
- (8) Teter, D. M.; Gibbs, G. V.; Boisen, M. B., Jr.; Allan, D. C.; Teter, M. P. *Phys. Rev. B* **1995**, *52*, 8064.
- (9) Liu, F.; Garofalini, S. H.; King-Smith, D.; Vanderbilt, D. *Phys. Rev. B* **1994**, *49*, 12528.
- (10) Holm, B.; Ahuja, R. *J. Chem. Phys.* **1999**, *111*, 2071.
- (11) Civalleri, B.; Zicovich-Wilson, C. M.; Ugliengo, P.; Sounders, V. R.; Dovesi, R. *Chem. Phys. Lett.* **1998**, *292*, 392.
- (12) Jeanvoine, Y.; Ángyán, J. G.; Kresse, G.; Hafner, J. *J. Phys. Chem. B* **1998**, *102*, 5573.
- (13) Shah, R.; Gale, J.; Payne, M. C. *J. Phys. Chem.* **1996**, *100*, 11688.
- (14) Hohenberg, P.; Kohn, W. *Phys. Rev.* **1964**, *136*, B864.
- (15) Kohn, W.; Sham, L. *Phys. Rev.* **1965**, *140*, A1133.
- (16) Payne, M. C.; Teter, M. P.; Allan, D. C.; Arias, T. A.; Joannopoulos, J. D. *Rev. Mod. Phys.* **1992**, *64*, 1045.
- (17) Kresse, G.; Hafner, J. *Phys. Rev. B* **1993**, *45*, 558.
- (18) Kresse, G.; Hafner, J. *Phys. Rev. B* **1994**, *49*, 14251.
- (19) Kresse, G.; Furthmüller, J. *Phys. Rev. B* **1996**, *54*, 11169.
- (20) Ceperley, D. M.; Alder, B. J. *Phys. Rev. Lett.* **1980**, *45*.
- (21) Perdew, J. P.; Chevary, J. A.; Vosko, S. H.; Jackson, K. A.; Pederson, M. R.; Singh, D. J.; Fiolhais, C. *Phys. Rev. B* **1992**, *46*, 6671.
- (22) Hamann, D. R. *Phys. Rev. Lett.* **1996**, *76*, 660.
- (23) Vanderbilt, D. *Phys. Rev. B* **1990**, *41*, 7892.
- (24) Kresse, G.; Hafner, J. *J. Phys.: Condens. Matter* **1994**, *6*, 8245.
- (25) Monkhorst, H. J.; Pack, J. D. *Phys. Rev. B* **1974**, *13*, 5188.
- (26) Froyen, S.; Cohen, M. L. *J. Phys. C: Solid State Phys.* **1986**, *19*, 2623.
- (27) Malvern, L. E. *Introduction to the Mechanics of a Continuous Medium*; Prentice Hall Inc.: Englewood Cliffs, NJ, 1969.
- (28) Levien, L.; Previtt, C. T.; Weidner, D. J. *Am. Mineral.* **1980**, *65*, 920.
- (29) Wright, A. F.; Lehmann, M. S. *J. Solid State Chem.* **1981**, *36*, 371.
- (30) Downs, R. T.; Palmer, D. C. *Am. Mineral.* **1994**, *79*, 9.
- (31) McSkimin, H. J.; Andreatch, P., Jr.; Thurston, R. N. *J. Appl. Phys.* **1965**, *36*, 1624.
- (32) Yeganeh-Haeri, A.; Weidner, D. J.; Parise, J. B. *Science* **1992**, *257*, 650.
- (33) Baerlocher C.; Meier W. M.; Olson D. H. *Atlas of Zeolite Framework Types*, 5th ed.; Elsevier: Amsterdam, 2001.
- (34) Filippone, F.; Buda, F.; Iarlori, S.; Moretti, G.; Porta, P. *J. Phys. Chem.* **1995**, *99*, 12883.
- (35) Richardson, J. W.; Pluth, J. J.; Smith, J. V.; Dytrych, W. J.; Bibby, B. M. *J. Phys. Chem.* **1988**, *92*, 243.
- (36) Knorr, K.; Braunbarth, C. M.; van de Goor, G.; Behrens, P.; Griewatsch, C.; Depmeier, W. *Solid State Commun.* **2000**, *11*, 503.
- (37) Zones, S. I.; Van Nordstrand, R. A. *Zeolites* **1988**, *8*, 166.
- (38) Alberti, A.; Davoli, P.; Vezzalini, G. Z. *Z. Kristallogr.* **1986**, *175*, 249.
- (39) Ito, M.; Yoshiko, S. *Bull. Chem. Soc. Jpn.* **1985**, *58*, 3035.
- (40) Reed, T. B.; Breck, D. W. *J. Am. Chem. Soc.* **1956**, *78*, 5972.
- (41) Kerr, G. T. *Inorg. Chem.* **1966**, *5*, 1537.
- (42) Astala, R.; Auerbach, S. M. *J. Am. Chem. Soc.* **2004**, *126*, 1843.
- (43) Olson, D. H.; Kokotailo, G. T.; Lawton, S. L.; Meier, W. M. *J. Phys. Chem.* **1981**, *85*, 2238.
- (44) van Koningsveld, H.; van Bekkum, H.; Jansen, J. C. *Acta Crystallogr. B* **1987**, *43*, 127.
- (45) van Koningsveld, H. *Acta Crystallogr. B* **1990**, *46*, 731.
- (46) Wu, E. L.; Lawton, S. L.; Olson, D. H.; Rohrman, A. C., Jr.; Kokotailo, G. T. *J. Phys. Chem.* **1979**, *83*, 2777.
- (47) Wang, Z.; Lambros, J.; Lobo, R. F. *J. Mater. Sci.* **2002**, *37*, 2491.
- (48) Johnson, G. K.; Tasker, I. R.; Howell, D. A.; Smith, J. V. *J. Chem. Thermodyn.* **1987**, *19*, 617.
- (49) Piccione, P. M.; Laberty, C.; Yang, S.; Cambor, M. A.; Navrotsky, A.; Davis, M. E. *J. Phys. Chem. B* **2000**, *104*, 10001.
- (50) Petrovic, I.; Navrotsky, A.; Davis, M. E.; Zones, S. I. *Chem. Mater.* **1993**, *5*, 1805.
- (51) Henson, N. J.; Cheetham, A. K.; Gale, J. D. *Chem. Mater.* **1994**, *6*, 1647.
- (52) Hammonds, K. D.; Heine, V.; Dove, M. T. *J. Phys. Chem. B* **1998**, *102*, 1759.
- (53) Kramer, G. J.; Farragher, N. P.; van Beest, B. W. H.; van Santen, R. A. *Phys. Rev. B* **1991**, *43*, 5068.
- (54) Sanders, M. J.; Leslie, M.; Catlow, C. R. A. *J. Chem. Soc., Chem. Commun.* **1984**, 1271.
- (55) Keskar, N. R.; Chelikowsky, J. R. *Phys. Rev. B* **1993**, *48*, 16227.